Plasma Sources Science and Technology

LETTER

Tomography-based spatial uniformity diagnostics for meter-sized plasmas

Letters

IOP Publishing

Plasma Sources Science and Technology

Plasma Sources Sci. Technol. **27** (2018) 10LT01 (8pp)

https://doi.org/10.1088/1361-6595/aac671

Letter

Tomography-based spatial uniformity diagnostics for meter-sized plasmas

Juhyeok Jang[1], Sanghoo Park[2], Joo Young Park[1] and Wonho Choe[1,2]

[1] Department of Physics, Korea Advanced Institute of Science and Technology, 291 Daehak-ro, Yuseong-gu, Daejeon 34141, Republic of Korea
[2] Department of Nuclear and Quantum Engineering, Korea Advanced Institute of Science and Technology, 291 Daehak-ro, Yuseong-gu, Daejeon 34141, Republic of Korea

E-mail: wchoe@kaist.ac.kr

Received 18 February 2018, revised 30 April 2018
Accepted for publication 21 May 2018
Published 9 October 2018

Abstract

Optical emission spectral tomography diagnostics have been developed to measure the spatial uniformity of meter-sized processing plasmas. The lines of sight and detector location are selected based on tomographic reconstruction tests using synthetic (phantom) images. The developed collection optics system is composed of slits, a plano-convex lens, optical interference filters and photodiode arrays. Using the collection optics, the line-integrated emission intensity is acquired from a meter-sized rectangular argon plasma (inductively coupled plasma at a frequency of 13.56 MHz), which was developed for display panel manufacturing. From the measured intensity, two-dimensional (2D) spatial distributions of argon atomic line intensity (675.3 nm and 852.1 nm) are obtained via the tomographic reconstruction technique based on the Phillips–Tikhonov regularization. In addition, 2D profiles of the electron excitation temperature (T_{exc}) are obtained from those of Ar intensity at the wavelengths 675.3 nm and 852.1 nm via two line method (in essence, a Boltzmann plot). The 2D argon plasma emission and T_{exc} profiles match well with the shape of the electrode and etch rate profile.

Keywords: etching, optical emission spectroscopy, tomography, plasma uniformity

1. Introduction

As large throughputs and low production costs are key requirements in microelectronics (*i.e.*, display panel and semiconductor) industries, the size of the processing equipment has increased along with that of the substrate. For this reason, a real-time monitoring or inspection of process uniformity has become critical for each process step in microelectronics manufacturing, especially in plasma processing. Plasma-based material processing such as deposition, etching and surface treatment have been an integral part in such manufacturing, and likewise, the size of the plasma chamber has increased. Because the electron characteristics directly govern the concentration of reactive species and the reaction rate in plasmas, which determine the processing performance such as etch or deposition rates [1–3], monitoring the spatial uniformity of the plasma characteristics is an essential part of plasma-based material processing. As the plasma size reaches the scale of multiple meters, the measurement of the spatial plasma uniformity becomes more challenging [4, 5]; for example, the set of local measurements at various positions by scanning methods are required to obtain spatial information of the plasma using conventional electrical probes. Two-dimensional (2D) probe systems have been developed [6, 7], however, the application of such systems to meter-sized plasmas is still a difficult issue.

Optical emission spectroscopy (OES) has been commonly employed as a non-invasive diagnostic method for a wide range of plasmas, including industrial plasmas. This technique is incredibly useful because of its non-intrusive nature that does not perturb the plasma, but it is difficult to directly obtain the spatially resolved information because the data acquired by the

detector are space-integrated emission intensity along the lines of sight. To resolve this measurement issue, adjustable lens optics [8] and tomography diagnostics [9, 10] were suggested. The tomography technique, which mathematically reconstructs the local intensity from the set of line-integrated emission data, is sufficiently powerful for visualizing the inner plasma structure. This technique has been well-established and actively used in medicine [11] and astronomy fields [12, 13]. Tomography technique has been also employed for fusion plasma diagnostics, particularly cross-sectional x-ray imaging [14–19] and bolometers [20, 21].

Here we demonstrate that a tomographic reconstruction using the Phillips–Tikhonov (P–T) regularization [22, 23] enables the monitoring of the 2D spatial uniformity of meter-scale industrial plasmas. Based on reconstruction tests using the synthetic profiles expected in the measurement, the detector with collection optics and their lines of sight were designed and the reconstruction accuracy of diagnostic system was examined. In addition, this system was especially prepared for measuring the 2D profile of the electron excitation temperature (T_{exc}), which is directly related to the electron temperature (T_e) [24]. Using the tomography diagnostics, in a meter-sized argon (Ar) plasma, 2D cross-sectional images of two Ar I atomic line emissions and T_{exc} were reconstructed, and these profiles match well with the etch rate results.

2. Tomographic reconstruction for 2D plasma diagnostics

2.1. Background theory and algorithm of tomographic reconstruction

In optical emission spectroscopy (OES), plasma emission measured outside the chamber is spatially integrated along the line-of-sight of the collection optics, thus the measured data is represented by line integrals. Several numerical approaches have been introduced to address the line-integration problem of OES. Among them, the tomographic reconstruction technique is most suitable to obtain cross sectional information on large-sized plasmas. In a 2D reconstruction space, the plasma emission is expressed by a discretized function, *i.e.,* emission intensity on each pixel (hereafter, referred to as a 'plasma pixel'), and the line-integrated signal $\vec{\mathbf{p}}$ can be expressed as the matrix product of the local emission $\vec{\mathbf{f}}$ and system (weight) matrix $\overleftrightarrow{\mathbf{W}}$:

$$\vec{\mathbf{p}} = \overleftrightarrow{\mathbf{W}} \cdot \vec{\mathbf{f}}. \tag{1}$$

It is noted that both $\vec{\mathbf{p}}$ and $\vec{\mathbf{f}}$ are column vectors. The system matrix $\overleftrightarrow{\mathbf{W}}$ contains the geometrical information of the line-of-sight, *i.e.*, the weight of local emission in the line-integrated data. The element of system matrix, w_{ij}, is defined as the length between intersections of the ith line-of-sight and jth plasma pixel. In most cases, because the number of plasma pixels is much larger than that of lines-of-sight (or detector channels), the system matrix has no inverse matrix, thus, equation (1) becomes an ill-conditioned problem.

The P–T regularization is one of the well-known reconstruction techniques for ill-conditioned problems and was used in this study to determine the solution of equation (1) for minimizing the weighted sum $\Phi = M^{-1} \| \vec{\mathbf{p}} - \overleftrightarrow{\mathbf{W}} \cdot \vec{\mathbf{f}} \|^2 + \eta \| \overleftrightarrow{\mathbf{L}} \cdot \vec{\mathbf{f}} \|^2$, where M is the number of detector channels. The first term is the squared distance between the measured data $\vec{\mathbf{p}}$ and line-integrated solution $\overleftrightarrow{\mathbf{W}} \cdot \vec{\mathbf{f}}$, and the second term represents the spatial variation of the solution. A Laplacian matrix $\overleftrightarrow{\mathbf{L}}$ represents the discretized second-order derivative between adjacent plasma pixels. The weight between the two terms in Φ is controlled by a regularization parameter η. If η is smaller than the optimal value, the solution will become unstable for the case of large gradients in the emission profile and will be largely contaminated by measurement noise, whereas with a larger η, the solution will become over-smoothened from the original profile, resulting in an inaccurate reconstruction. The optimal value of η was determined by the generalized cross validation technique, which is found in [25, 26]. After singular value decomposition of $\overleftrightarrow{\mathbf{W}} \cdot \overleftrightarrow{\mathbf{L}}^{-1}$, as described in [27, 28], the P–T solution that minimizes Φ can be obtained as follows:

$$\vec{\mathbf{f}}_{P\text{-}T}(\eta) = (\overleftrightarrow{\mathbf{W}}^T \cdot \overleftrightarrow{\mathbf{W}} + M\eta \overleftrightarrow{\mathbf{L}}^T \cdot \overleftrightarrow{\mathbf{L}})^{-1} \overleftrightarrow{\mathbf{W}}^T \cdot \vec{\mathbf{p}}. \tag{2}$$

2.2. Reconstruction test using artificial intensity profiles

A tomography diagnostic system was developed for monitoring an industrial inductively coupled etching plasma, whose geometry is shown in figure 1(a). The sizes of the inner wall of the chamber and the bottom electrode (known as the susceptor) are $3.3 \times 3.0\,m^2$ and $2.6 \times 2.2\,m^2$, respectively. The gap distance between the top and bottom electrodes is 0.35 m. Ten viewports were prepared and used for this diagnostic system, as denoted by red triangles in the figure.

To assess the reconstruction performance of the developed computer tomography code, reconstruction tests were conducted using synthetic (called phantom) images with square-shaped flat and hollow profiles (see figures 1(b), (c)), which are the most expected profiles in our experiment. The basis of the phantom was assumed to cover the whole electrode area, which is denoted by magenta dashed lines in the figure. The reconstruction area inside the chamber was divided into 67×61 plasma pixels with each size of $50 \times 50\,mm^2$. Two kinds of reconstruction errors, that is, the reconstruction error for the jth plasma pixel (e_j) and the root-mean-square error (e_{rms}) over the whole plasma, were defined to determine the reconstruction accuracy in our diagnostic configuration and numerical code as follows:

$$e_j(\%) = \left| \frac{f_{ph,j} - f_{rec,j}}{f_{ph,j}} \right| \times 100, \tag{3}$$

$$e_{rms}(\%) = \frac{\| \vec{\mathbf{f}}_{ph} - \vec{\mathbf{f}}_{rec} \|}{\| \vec{\mathbf{f}}_{ph} \|} \times 100, \tag{4}$$

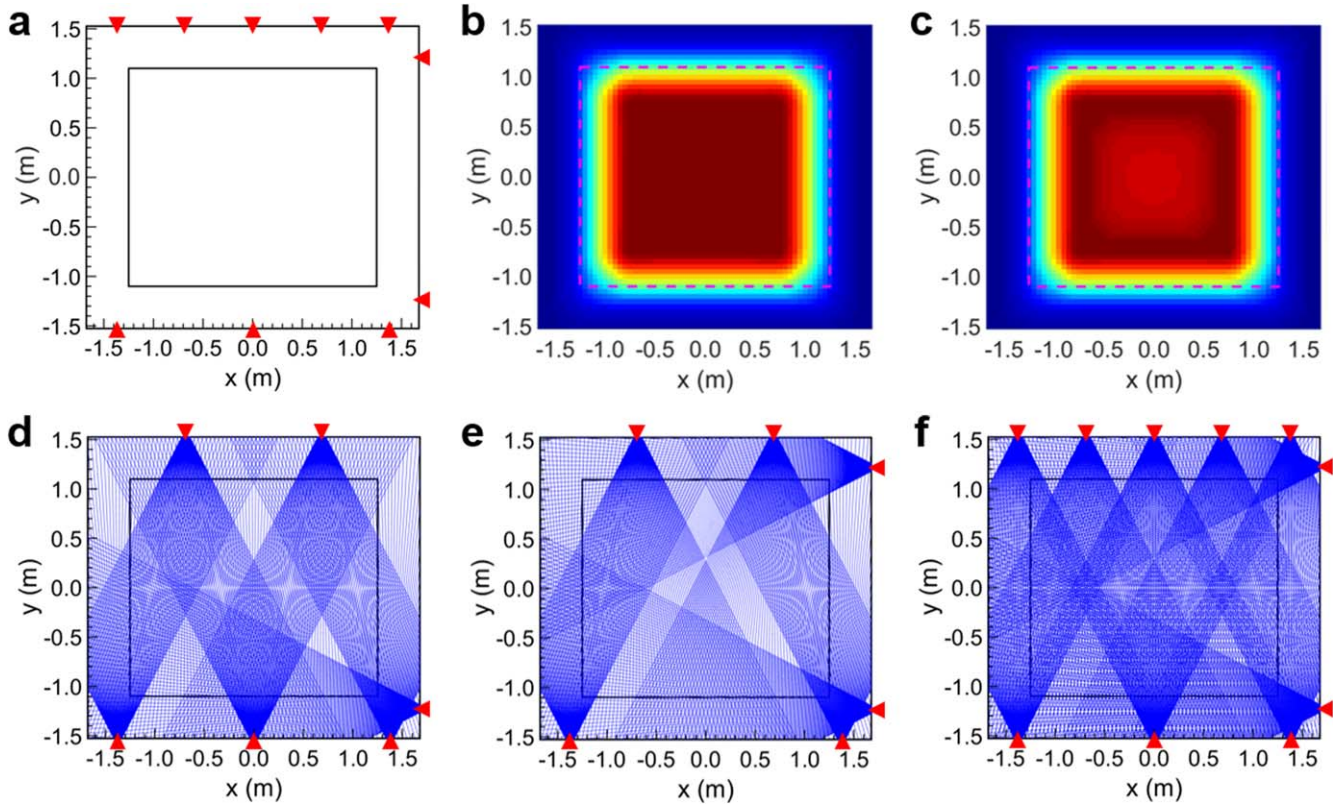

Figure 1. (a) Cross-sectional schematic of meter-sized industrial etching chamber. The inner contour represents the boundary of the electrode, and the position of the available viewports are depicted as red triangles on the vacuum chamber wall. Two fabricated plasma emission phantoms with (b) flat and (c) hollow square structures. The magenta dashed lines represent the electrode. Phantom reconstruction tests were performed with three cases of detector alignments: (d) case I: five vertical viewing arrays and one horizontal viewing array, (e) case II: four vertical viewing arrays and two horizontal viewing arrays, and (f) case III: all ten available arrays.

where $\overrightarrow{\mathbf{f}}_{\mathrm{ph}}(f_{\mathrm{ph},j})$ and $\overrightarrow{\mathbf{f}}_{\mathrm{rec}}(f_{\mathrm{rec},j})$ are the column vectors (their elements) of the phantom and reconstructed images, respectively. The three different sets of detector arrays depicted in figures 1(d)–(f) were used for the reconstruction tests and each result will be discussed in the following.

Figures 2(a)–(c) show the reconstruction test results for the flat profile with the different sets of detectors in figures 1(d)–(f), respectively. The leftmost and center images present the reconstructed phantom images and e_j distribution for each case, and 1D profiles of the reconstruction result at $x = 0$ are presented in the rightmost graphs. For the first case in figure 2(a), five vertically aligned arrays and one horizontally aligned array are used. Although e_{rms} is 15.7%, there is a large asymmetry to $y = 0$ and we have e_j of approximately 30% near $y = 800$ mm. This is because only one array was used for the horizontal view, resulting in a lack of horizontal information for the reconstruction. In the second case shown in figure 2(b), the use of one additional port in the right-side of the chamber improves the reconstruction in the aforementioned asymmetry so much that e_{rms} and e_j near $y = 800$ mm decrease to 7.0% and 20%, respectively. In the third case (figure 2(c)), using all available viewports of the chamber, the reconstruction image is the closest to the phantom with 5.0% of e_{rms}. The improvement in reconstruction accuracy with the increase in the number of detectors is clearly shown in the rightmost graphs.

The reconstruction results of the hollow profile are shown in figure 3, where the results exhibit behavior identical to those of the flat phantom. With only one horizontal viewing array, the hollow structure is not well-reconstructed ($e_{\mathrm{rms}} = 16.5\%$), as shown in figure 3(a). In the case of the two horizontal viewing arrays depicted in figure 3(b), the reduction in the reconstruction error is distinct, allowing the hollow structure to be clearly reconstructed, and e_{rms} decreases from 16.5 to 7.5%. A more accurate reconstruction with 5.2% of e_{rms} is achieved by using all viewports (see figure 3(c)). As demonstrated in figures 2 and 3, using all 10 viewports yields the best reconstruction performance available in this geometry. However, the detector arrangement shown in figure 1(e) was employed in the experiment because of the experimental availability of the viewports.

Noise, which is induced by various sources such as electromagnetic interference and stray current in the detector, is unavoidable and strongly affect the reconstruction process. To evaluate the reconstruction accuracy in the presence of noise, reconstruction tests were also performed by adding random noise to the line-integrated signal of each phantom. The level of random noise was 0%–10.0% of the maximum value in the line-integrated signal (acceptable range of noise level induced by a photodiode itself). The arrangement of detectors given in figure 1(e) was used. For each level of

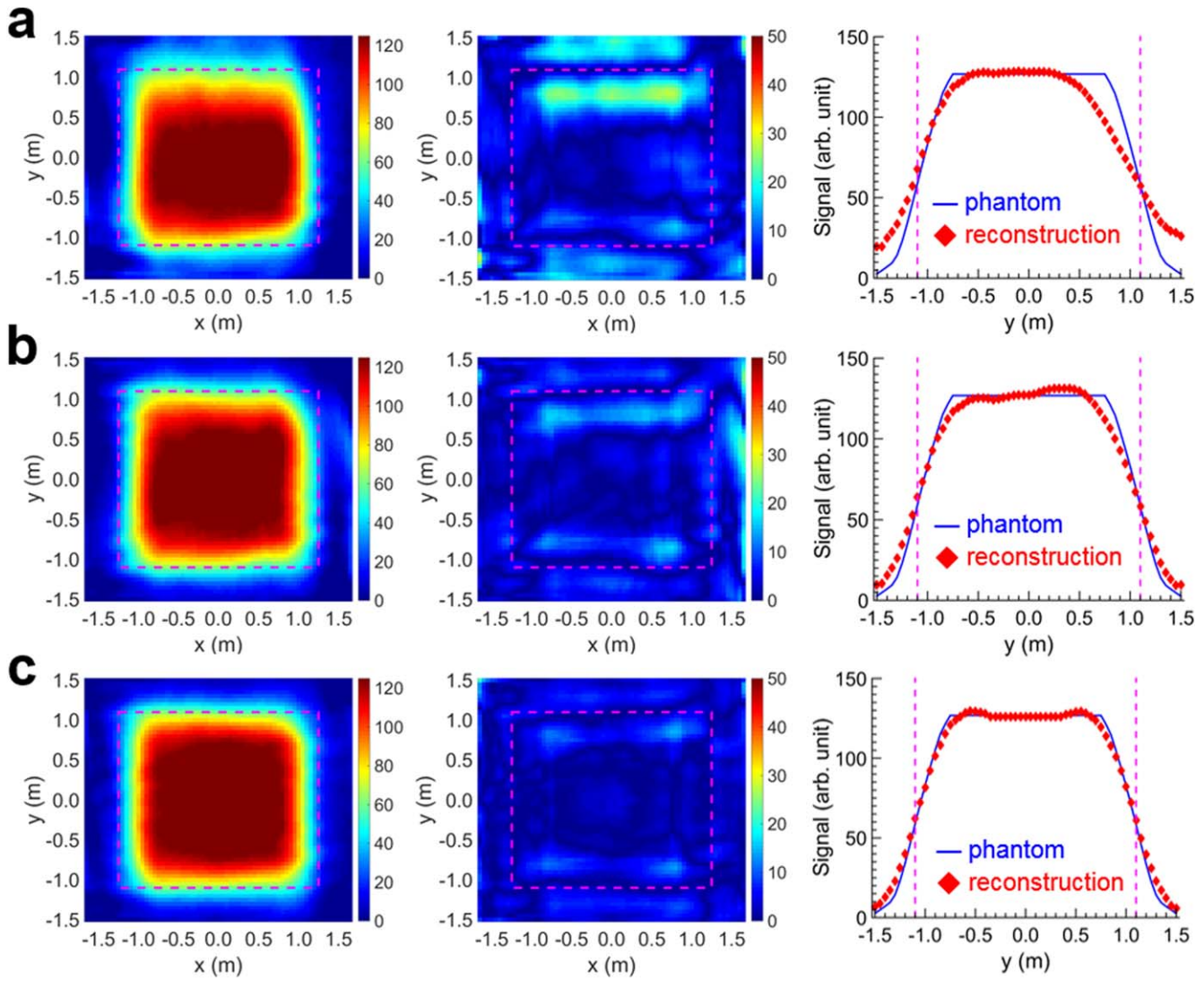

Figure 2. Phantom reconstruction test results with the flat square phantom. Comparison of three cases of detector array arrangements: (a) case I, (b) case II, and (c) case III in figure 1. The left figures illustrate the reconstruction images corresponding to each arrangement. The magenta dashed lines denote the electrode boundary. The middle figures represent the reconstruction error (e_i) between the phantom and reconstructed images . The color scales are normalized to 50%. The right figures show the one-dimensional plots of the phantom (blue solid lines) and reconstructed profiles (red diamonds) on x = 0.

random noise, reconstruction tests were performed 100 times to evaluate the mean value ($\langle e_{\rm rms}\rangle$) and standard deviation ($\sigma_{\rm rms}$) of $e_{\rm rms}$. As the random noise increased from 0 to 10.0%, $\langle e_{\rm rms}\rangle$ and $\sigma_{\rm rms}$ for the flat phantom gradually increased from 7.0 to 12.4% and from 0 to 2.7%, respectively. For the hollow phantom, $\langle e_{\rm rms}\rangle$ increased from 7.5 to 12.8% and $\sigma_{\rm rms}$ increased from 0 to 3.0%. Because the signal to noise ratio of our detector does not exceed 10%, the expected levels of $\langle e_{\rm rms}\rangle$ and $\sigma_{\rm rms}$ for real plasma are expected to be less than 12.8% and 3.0%, respectively.

3. Experimental

3.1. Tomography diagnostic system

A detector system was developed for the 2D reconstruction of cross-sectional emission profiles from a 2.6 × 2.2 m^2-sized industrial plasma (manufactured by LIG INVENIA Co.). A schematic of the detector assembly is presented in figure 4(a). Each detector unit is directly attached to the viewport of the chamber. Figure 4(b) shows inner components of the detector assembly. Plasma emission passes through a 0.1 mm × 1.0 mm^2 (width × height) slit. In order to make the incident angle of plasma emission normal to the optical interference filter, a plano-convex lens (#45-715, Edmund Optics), which has a back focal length of 43.28 mm, is placed immediately behind the slit. Optical interference filters that have center wavelengths of 676 nm (#65-234, Edmund Optics) and 850 nm (#67-919, Edmund Optics) with a full-width at half-maximum of 10 nm are used to transmit Ar I atomic line emission at wavelengths 675.3 nm and 852.1 nm, respectively. Emission intensities at the two wavelengths were measured sequentially by changing the filters that were installed at the linear-motion slide. Photo-diode arrays (S8865-128, Hamamatsu Photonics) were used as

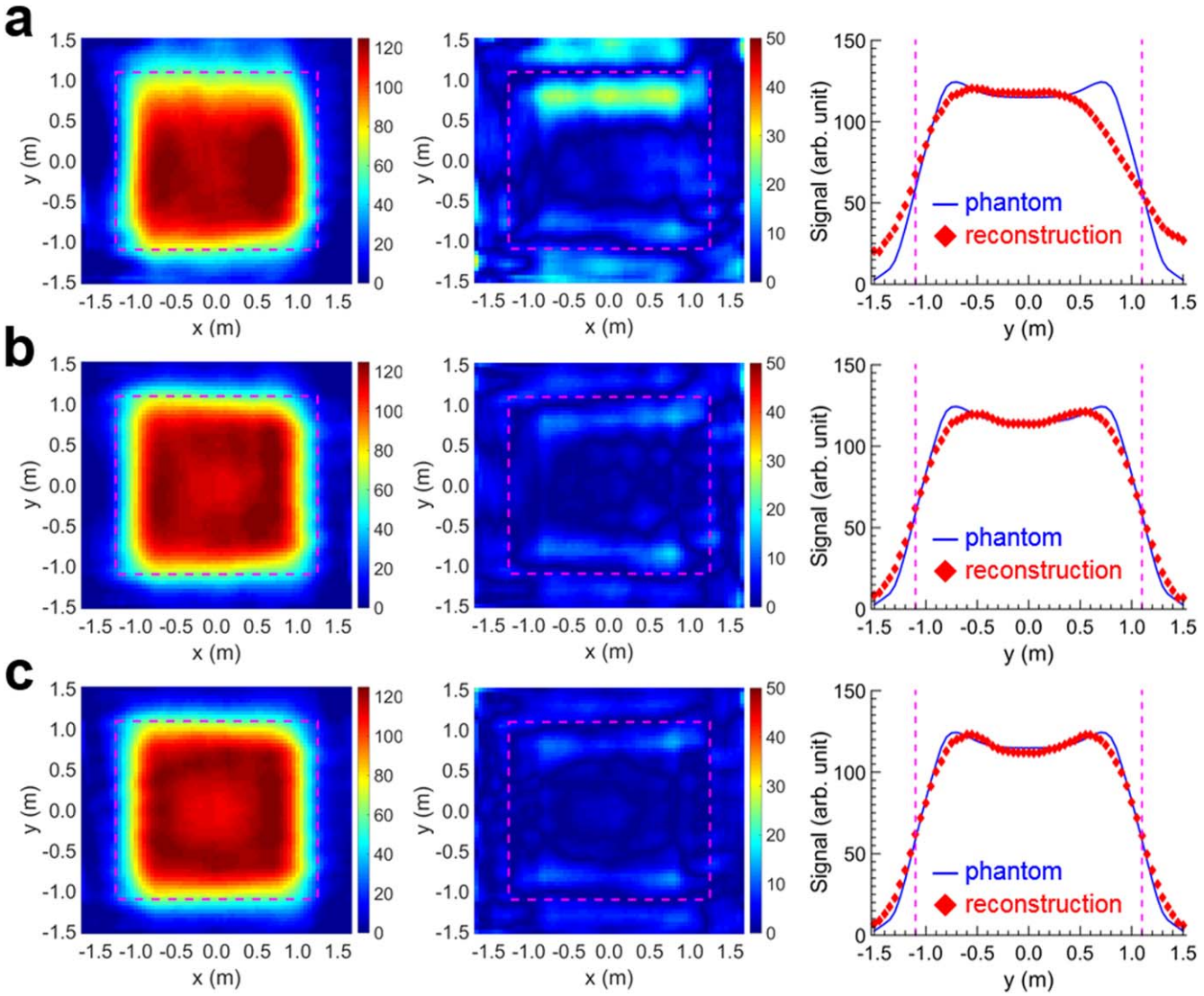

Figure 3. (a)–(c) Phantom reconstruction test results with the hollow square phantom for cases I, II, and III, respectively.

detectors. For the tomography diagnostics, photodiode arrays are quite suitable because of its high spatial and temporal resolutions, which are key requirements toward achieving the real-time monitoring of plasma processing, with respect to the compact size. For each viewport, 78 channels (*i.e.,* 78 lines of sight) of the detector were available because of the geometrical accessibility of the chamber structure, and the lines of sight for the diagnostic system were designed to maximize the viewing angle in the plasma. The time resolution was 80 Hz. Driver circuits (C9118-01, Hamamatsu Photonics) were used to amplify the output photocurrent from the detector. The relative calibration of each detector system for 675.3 nm and 852.1 nm was performed using a combination of an opal glass (as a Lambertian diffuser, #46-106, Edmund Optics) and commercial tungsten lamp.

A schematic diagram of the integrated diagnostic system is shown in figure 4(c). The data flows between each part are depicted by black arrows. The function generator (33500B, Agilent) provides a 50-kHz sync signal and 12.5-Hz reset signal to the first detector, and these signals are transferred serially from the first to last detector for the simultaneous integration of channels. The cascade readout provides the serial output of the detectors, *i.e.*, a packet of intensity signal, in the opposite direction of the input signal. The serial output generated by the first detector is delivered to the data acquisition device (cDAQ-9178, National Instruments). The control of the integrated system and data acquisition were performed using the LabVIEW.

3.2. Excitation temperature measurement

The excitation temperature characterizes the excitation level of bound electrons in the overall atom in the plasma. The population of atoms in the m state, f_m, can be expressed with the Boltzmann relation as

$$f_m = \frac{N}{Z(T_{\mathrm{exc}})} g_m \exp\left(-\frac{E_m}{k_{\mathrm{b}} T_{\mathrm{exc}}}\right), \tag{5}$$

where E_m and g_m are the energy level and statistical weight of the atom in m state, respectively. N is the number of atoms, Z

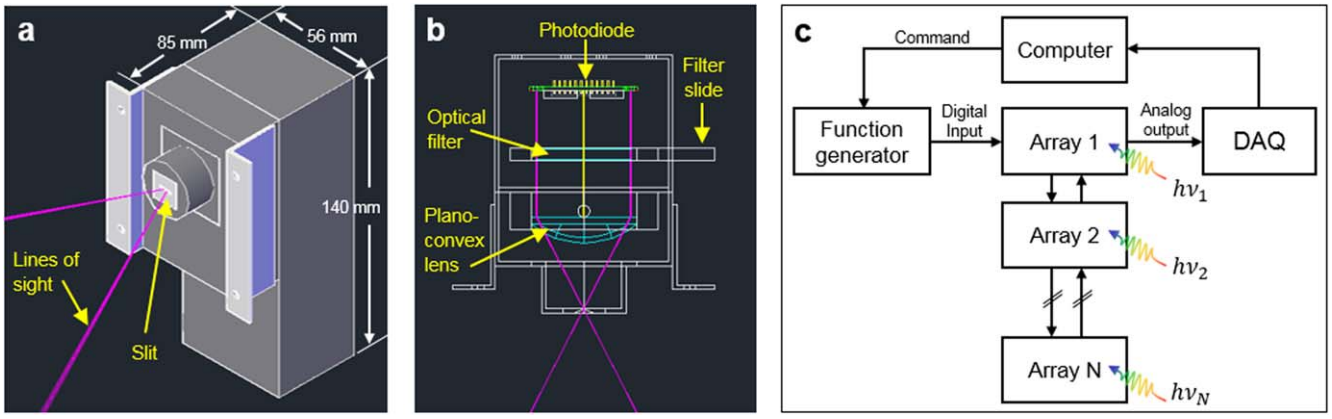

Figure 4. (a) CAD drawing of the spectral tomography detector array, and (b) inner structure of the detector unit. The magenta lines denote the range of the lines of sight. (c) Diagram of the entire diagnostic system data flow. The input for the photodiode array is provided by a function generator. Each array exchanges input and output signals. The final output goes to the data acquisition device (DAQ).

is the partition function, and k_b is the Boltzmann constant. While a transition from the m to n state occurs, the emissivity $I_{m,n}$ can be expressed as [29]

$$I_{m,n} = f_m A_{m,n} \frac{hc}{\lambda}, \tag{6}$$

where $A_{m,n}$ is the transition probability from the upper m to lower n state, h and c are the Planck constant and speed of light, respectively, and λ represents the wavelength of the corresponding energy difference between the m and n states. By substituting equation (5) into equation (6), we obtain

$$I_{m,n} = \frac{hc}{\lambda} \frac{NA_{m,n} g_m}{Z(T_{exc})} \exp\left(-\frac{E_m}{k_b T_{exc}}\right). \tag{7}$$

This relation can be rewritten as

$$\ln\left(\frac{I_{m,n}\lambda}{A_{m,n}\, g_m}\right) = -1.4388 \times \frac{E_m}{T_{exc}} + \text{const.} \tag{8}$$

It is noted that the Boltzmann plot, *i.e.*, the plot of the left hand side of equation (8) versus E_m, yields T_{exc}. Figure 5 shows the Boltzmann plot that produced from the space- and time-integrated emission spectrum of Ar plasma (black circles) in the same chamber, as an example. A linear fitting for 12 Ar atomic lines (a black dotted line) yields 1.82 eV of T_{exc}. In this work, more simply, two Ar I lines at the wavelengths 675.3 nm and 852.1 nm were selected to obtain T_{exc}. We derived the simple relation between the two lines and T_{exc}(so called two line method) from equation (7) as

$$\frac{I_{m_1,n_1}}{I_{m_2,n_2}} = \left(\frac{\lambda_2 A_{m_1,n_1} g_{m_1}}{\lambda_1 A_{m_2,n_2} g_{m_2}}\right) \exp\left(-1.4388 \times \frac{E_{m_1} - E_{m_2}}{T_{exc}}\right), \tag{9}$$

where indices 1 and 2 represent each atomic line, respectively. $I_{m_1,n_1}/I_{m_2,n_2}$ is the ratio between reconstructed relative intensities for each plasma pixel and other parameters except T_{exc} are known for Ar. Thus, T_{exc} profile can be obtained as intensity profiles of two atomic lines are reconstructed. It is worth noting that the fitted slope of these two lines (a red line) in the Boltzmann plot is well matched with that of all data, as depicted in figure 5.

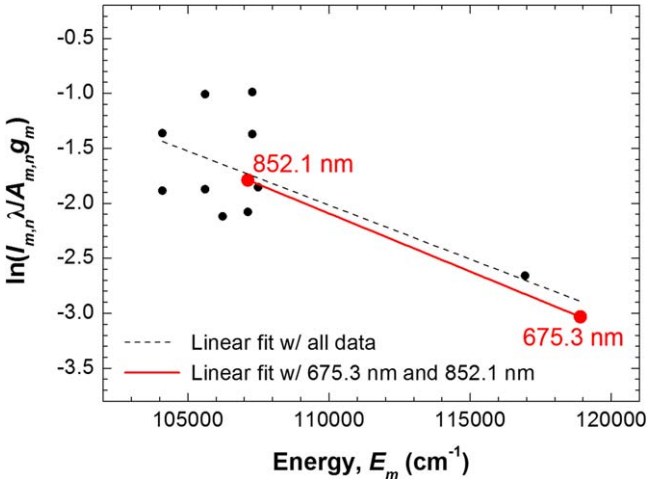

Figure 5. The Boltzmann plot of 12 Ar I lines (black and red circles). The black dashed line represents linear fitting for all Ar I lines, which yields 1.82 eV of T_{exc}. Red circles and the red line represent two Ar I lines at 675.3 nm and 852.1 nm and their linear fitting, respectively. The slope of red line yields 1.69 eV of T_{exc}.

4. Results and discussion

Ar plasma emission was measured in the eighth-generation industrial etching plasma device described in the previous section. The same plasma pixels for the phantom reconstruction tests were used for the reconstruction of the experimental data. Six detector arrays were used for the measurement whose space and time resolutions were 5 cm and 80 Hz, respectively. The flow rate of Ar gas was fixed at 2800 standard cubic centimeters per minute and the gas pressure was maintained at 100 mTorr. The input power of 8 kW at 13.56 MHz rf was provided to the plasma. The images shown in figures 6(a), (b) are the tomographically reconstructed 2D emission profiles of the 675.3 and 852.1 nm neutral Ar I emissions, respectively. The dashed square represents the boundary of the bottom electrode. The bright regions of the reconstructed images match well with the electrode area, on which plasma mainly exists.

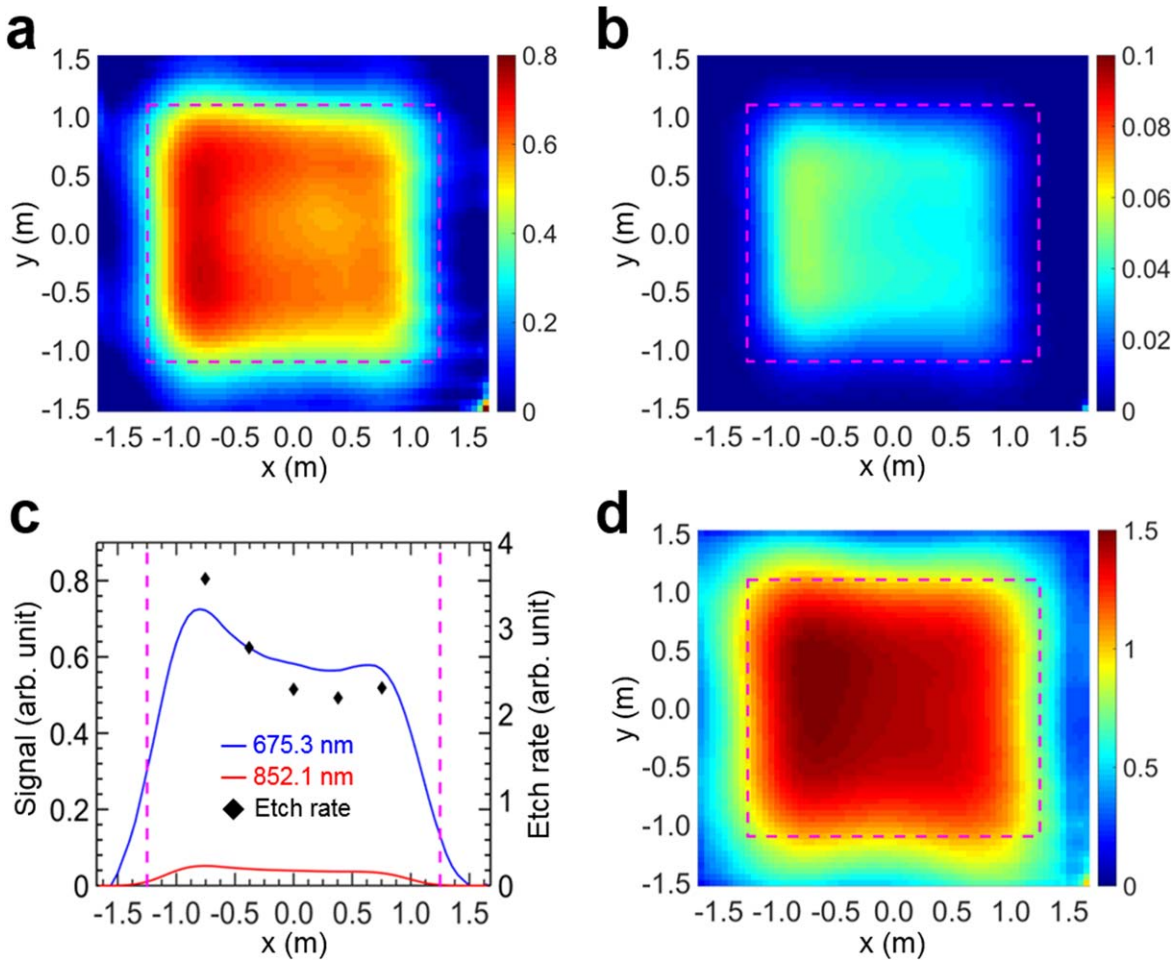

Figure 6. 2D images of plasma radiation at wavelengths of (a) 675.3 and (b) 852.1 nm in arbitrary unit. It is noted that the color scale of (b) is 8 times lower than that of (a). (c) Horizontal profiles of plasma radiation on y = 0 mm. The blue and red curves denote the profiles of 675.3 and 852.1 nm, respectively. The black diamonds denote the five-point measurement of the etch rate. (d) 2D excitation temperature profile in eV. Magenta dashed lines denote the electrode boundary.

As shown in figure 6(c), the plasma emission profiles have a weak hollow structure, and those are compared to the etch profile (denoted by black scatters) of the SiO_2 wafer in Ar/NF_3 plasma with the rf input power of 10 kW. The etch profile shows an asymmetric structure similar to the reconstructed emission profile. This result suggests that the tomography technique can be effectively used as a monitoring tool for material processing in large meter-sized plasmas instead of conventional methods such as electrical probes, which are unfavorable to those large plasmas.

Depicted in figure 6(d) is the 2D T_{exc} profile obtained using the reconstructed emission profiles of the two aforementioned wavelengths. In this operation, the maximum value of T_{exc} reaches 1.5 eV. The T_{exc} profile also shows a square-shaped hollow structure similar to the plasma emission presented in figures 6(a), (b). In our previous studies, the T_{exc} profile was a good representation of T_e as the ratio between T_{exc} and T_e remained constant in rf plasmas in certain operational ranges [24]. With further studies on the factor of T_{exc}/T_e, spectral tomographic reconstruction will be an attractive diagnostic tool for the *in situ* monitoring of the spatial uniformity of T_e during plasma processes. The non-zero signal outside the electrode in figure 6(d) may come from the inaccuracy of the emission ratio because the plasma emission outside the electrode is too low for both wavelengths.

5. Conclusions

Spatial uniformity of plasma is one of critical factors in plasma-based material processing. As the size of cutting-edge plasma devices often reaches the scale of a few meters, the uniformity measurement using conventional probes is problematic in such plasmas. To address this issue, a non-invasive diagnostic system with a tomography technique was developed for a meter-sized etching chamber. The reliability of the developed tomography code was examined by phantom reconstruction tests with square flat and hollow profiles. A spectroscopic tomography diagnostic system was designed based on optimal lines of sight, which were determined by reconstruction tests. This diagnostic system in conjunction with the tomography code successfully reconstructed the 2D cross-sectional images of Ar emission and T_{exc} in the meter-

sized plasma chamber. The reconstructed images showed well-matched result with the etch rate profile. It is noted that the accuracy of the uniformity measurement shown in this paper can be further improved by using more number of viewports and thus more detector arrays as demonstrated in the phantom reconstruction tests.

Compared to conventional diagnostic methods, the spectroscopic tomography diagnostic system shows several merits. Firstly, as an overall time consumption of the tomography diagnostic system is up to 1 s, a real-time monitoring of plasma spatial uniformity is possible in meter-sized industrial plasma devices during material processing. Based on the cutting-edge detectors and optimized computer code, the diagnostic system can also be employed for fast detection of micro-arcs that can severely degrade the quality of material processing. Secondly, wavelength-resolved imaging allows us to identify various species including impurity ions or radicals in the plasma. The spectroscopic tomography detector can provide not only plasma uniformity and T_{exc}, but also crucial information of chemical reactions during material processing, such as end-point detection in chamber cleaning. Lastly, the same diagnostic system can be easily utilized for any size and geometry of the plasma by only modifying the system matrix without mechanical changes. It should be noted that the reconstruction test procedure in this paper is not limited to our case; it is also useful to find the optimal diagnostics design in given plasma configurations. Because of the aforementioned features, spectroscopic tomography diagnostics can be a valuable tool for plasma-based material processing at ultra-large scales.

Acknowledgments

The authors thank LIG INVENIA for allowing the authors perform their experiment at their eighth-generation processing plasma device. This work was supported by the Ministry of Trade, Industry and Energy of Korea (grant no. 10041867) and the National Research Foundation of Korea (NRF) funded by the Ministry of Science, ICT and Future Planning (NRF-2014M1A7A1A03045092).

ORCID iDs

Juhyeok Jang https://orcid.org/0000-0002-9991-6072
Sanghoo Park https://orcid.org/0000-0002-4180-7455
Joo Young Park https://orcid.org/0000-0002-4884-3301
Wonho Choe https://orcid.org/0000-0002-8952-8252

References

[1] Donnelly V M and Kornblit A 2013 *J. Vac. Sci. Technol.* A **31** 050825
[2] Kuo Y and Crowe J R 1990 *J. Vac. Sci. Technol.* A **8** 1529
[3] Ishijima T, Nojiri Y, Toyoda H and Sugai H 2010 *Jpn. J. Appl. Phys.* **49** 086002
[4] Tatsumi T, Hikosaka Y, Morishita S, Matsui M and Sekine M 1999 *J. Vac. Sci. Technol.* A **17** 1562
[5] Kuo Y 2008 *Jpn. J. Appl. Phys.* **47** 1845
[6] Howling A A, Derendinger L, Sansonnens L, Schmidt H, Hollenstein Ch, Sakanaka E and Schmitt J P M 2005 *J. Appl. Phys.* **97** 123308
[7] Setsuhara Y, Takenaka K, Ebe A and Nishisaka K 2007 *Plasma Process. Polym.* **4** S628–32
[8] Park H, Choe W and Yoo S J 2010 *Spectrochim. Acta* B **65** 1029
[9] Makabe T and Petrović Z Lj 2002 *Appl. Surf. Sci.* **192** 88
[10] Fadeev A V, Rudenko K V, Lukichev V F and Orlikovskii A A 2011 *Russ. Microelectron.* **40** 108
[11] Buzug T M 2008 *Computed Tomography: From Photon Statistics to Modern Cone-Beam CT* 1st edn (Berlin: Springer)
[12] VanderPlas J T, Connolly A J, Jain B and Jarvis M 2011 *Astrophys. J.* **727** 118
[13] Zhao J, Kosovichev A G and Sekii T 2010 *Astrophys. J.* **708** 304
[14] Granetz R S and Smeulders P 1988 *Nucl Fusion.* **28** 457
[15] Kim J and Choe W 2004 *Rev. Sci. Instrum.* **75** 3974
[16] Kim J, Lee S H and Choe W 2006 *Rev. Sci. Instrum.* **77** 10F513
[17] Lee S H, Kim J, Lee J H and Choe W 2010 *Curr. Appl. Phys.* **10** 893
[18] Lee S H, Jang J, Hong J, Pacella D, Romano A, Gabellieri L, Jang S, Kim J and Choe W 2014 *Rev. Sci. Instrum.* **85** 11E827
[19] Song I, Jang J, Jeon T, Pacella D, Claps G, Murtas F, Lee S H and Choe W 2016 *Curr. Appl. Phys.* **16** 1284
[20] Kallenbach A, Bernert M, Eich T, Fuchs J C, Giannone L, Herrmann A, Schweinzer J, Treutterer W and ASDEX Upgrade Team 2012 *Nucl. Fusion* **52** 122003
[21] Jang J, Choe W, Peterson B J, Seo D C, Mukai K, Sano R, Oh S, Hong S H, Hong J and Lee H Y 2018 *Curr. Appl. Phys.* **18** 461
[22] Tikhonov A N and Arsenin V Y 1977 *Solutions of Ill-Posed Problems* (Washington, DC: Winston & Sons)
[23] Honerkamp J and Weese J 1990 *Continuum Mech. Thermodyn.* **2** 17
[24] Park H, You S J and Choe W 2010 *Phys. Plasmas* **17** 103501
[25] Golub G H, Heath M and Wahba G 1979 *Technometrics* **21** 215
[26] Iwama N, Yoshida H, Takimoto H, Shen Y, Takamura S and Tsukishima T 1989 *Appl. Phys. Lett.* **54** 502
[27] Terasaki N, Hosoda Y, Teranishi M and Iwama N 1997 *Fusion Eng. Des.* **34-35** 801
[28] Ohdachi S, Toi K, Fuchs G and TEXTOR team and LHD Experimental Group 2006 *Plasma Sci. Technol.* **8** 45
[29] Moon S Y, Choe W, Uhm H S, Hwang Y S and Choi J J 2002 *Phys. Plasmas* **9** 4045